

ThermoNeRF: Multimodal Neural Radiance Fields for Thermal Novel View Synthesis

Mariam Hassan¹, Florent Forest¹, Olga Fink¹, and Malcolm Mielle²✉

¹ École Polytechnique Fédérale de Lausanne (EPFL)

`firstname.lastname@epfl.ch`

² Schindler AG

`firstname.lastname@schindler.com`

Abstract. Thermal scene reconstruction exhibit great potential for applications across a broad spectrum of fields, including building energy consumption analysis and non-destructive testing. However, existing methods typically require dense scene measurements and often rely on RGB images for 3D geometry reconstruction, with thermal information being projected post-reconstruction. This two-step strategy, adopted due to the lack of texture in thermal images, can lead to disparities between the geometry and temperatures of the reconstructed objects and those of the actual scene. To address this challenge, we propose ThermoNeRF, a novel multimodal approach based on Neural Radiance Fields, capable of rendering new RGB and thermal views of a scene jointly. To overcome the lack of texture in thermal images, we use paired RGB and thermal images to learn scene density, while distinct networks estimate color and temperature information. Furthermore, we introduce ThermoScenes, a new dataset to palliate the lack of available RGB+thermal datasets for scene reconstruction. Experimental results validate that ThermoNeRF achieves accurate thermal image synthesis, with an average mean absolute error of 1.5°C, an improvement of over 50% compared to using concatenated RGB+thermal data with Nerfacto, a state-of-the-art NeRF method. Code is available at <https://github.com/SchindlerEPFL/thermo-nerf>.

Keywords: Thermal Imaging · Neural Radiance Fields · 3D Reconstruction · Multimodality

1 Introduction

Since their introduction by Mildenhall et al. [40], Neural Radiance Fields (NeRFs) have achieved great success in 3D reconstruction and novel view synthesis and have been extended for diverse tasks such as depth estimation [9, 51], semantic segmentation [62, 34] and object detection [56, 24]. While most NeRF models learn an implicit representation of a scene from a sparse set of RGB images, NeRFs have also been successfully extended to other sensor modalities such as depth views [63], near-infrared and multi-spectral images [44], LiDAR point clouds [59, 63] and even audio signals [10]. Moreover, it has been demonstrated that NeRFs can learn from more than a single modality at a time—for example, Poggi et al. [44]

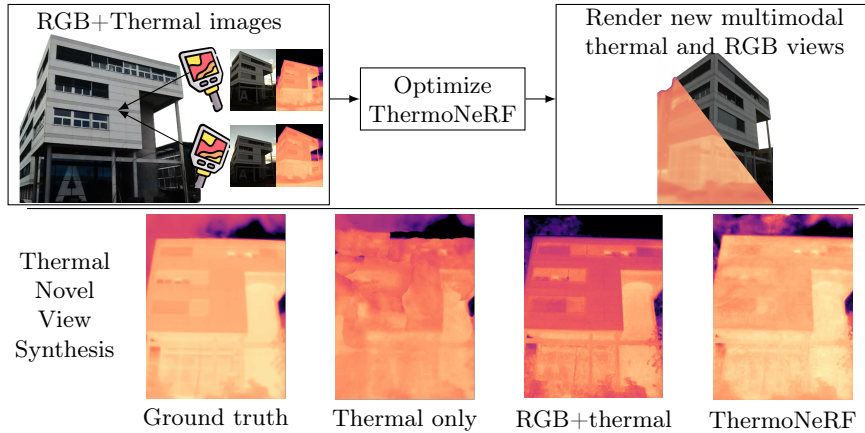


Fig. 1: We propose **ThermoNeRF**, a multimodal NeRF-based approach that takes paired thermal and RGB images as input and synthesizes novel views in both modalities. ThermoNeRF demonstrates enhanced thermal information estimation compared to non-multimodal methods, while preserving the quality of rendered RGB views.

combine near-infrared and RGB images to learn a more accurate representation of the scene than when using only one modality. However, multimodal NeRFs also often depend on the presence of salient or similar features between the modalities [44].

In this paper, we focus on multimodal NeRF using RGB and thermal imaging. Thermal cameras capture the radiation emitted by objects as a function of their temperature. At ambient temperature ranges, objects radiate in the mid- and far-infrared region of the electromagnetic spectrum. Since thermal radiation is scattered and reflected from various points within a scene, thermal images naturally lack texture and appear soft—i.e., with a low edge contrast—an effect known as ghosting [1]. Hence, despite the benefits of using 3D thermal representations in infrastructure inspection and monitoring [28, 22], non-destructive testing [22], and agriculture [43], such models are primarily constructed using photogrammetry, which requires large amounts of RGB data or advanced equipment [39, 15, 37]. Moreover, thermal images are often not considered during the geometric reconstruction, and temperature information is projected post-reconstruction [45], leading to potential discrepancies between the model and actual temperatures.

Additionally, the development of thermal scene reconstruction algorithms is hindered by the lack of benchmark datasets specifically designed for this task. Instead, the majority of existing datasets that include thermal images are focused on dynamic and changing environments for a variety of perception tasks, such as object detection [26, 18, 19], object tracking [5], face or object recognition [29, 12], semantic segmentation [52], motion estimation [14], SLAM [57] and autonomous driving [13, 32].

To address the gaps outlined above, we propose ThermoNeRF (**Thermographic NeRF**), the first multimodal NeRF model capable of rendering unseen views in

both RGB and thermal modalities jointly (see Fig. 1). The design of our approach is guided by the specific properties of thermal images. ThermoNeRF uses a shared density MLP that leverages the visual features of the RGB modality to learn the geometry of the scene while ensuring consistency with the thermal measurements. Color and thermal information are learned through decoupled MLPs, to prevent the influence of colors on the estimated temperatures, and vice-versa. In addition, we also introduce ThermoScenes, a new paired thermal-RGB dataset comprising ten diverse scenes—six indoor and four outdoor scenes—for 3D scene reconstruction and novel view synthesis.

Our contributions are summarized as follows:

- We propose ThermoNeRF, the first multimodal NeRF capable of rendering both thermal and RGB views jointly.
- We conduct extensive experiments to validate how ThermoNeRF’s architecture allows the RGB modality to guide the density estimation for thermal reconstruction while preventing interactions between color and estimated temperatures.
- We provide ThermoScenes, a new RGB+thermal image dataset for 3D scene reconstruction and novel view synthesis, featuring ten scenes with diverse temperature ranges, object types and sizes.
- Finally, we present a comprehensive evaluation of our method’s performance, covering both temperature estimation and reconstruction quality on unseen poses. Our results demonstrate improved temperature estimation with no loss in reconstruction fidelity when compared to models trained using only thermal images or concatenated RGB+thermal images as input.

2 Related Work

2.1 Thermal Computer Vision

Thermal cameras measure thermal radiation emitted by any matter with a temperature above absolute zero Kelvin. While most practical temperature ranges fall within the infrared (IR) region of the electromagnetic spectrum [25], thermal cameras operate in the mid- to far-IR spectrum, unlike near-infrared (NIR) sensors, which work closer to the visible range. It is important to note that thermal cameras also detect thermal radiations that are scattered and reflected by objects and the environment, resulting in thermal images that are naturally textureless and soft—a phenomenon known as the ghosting effect [1]. While researchers have explored object detection [17] and tracking [6] using infrared sensors, as well as the analysis of thermal images [27, 36, 35], due to their soft and textureless nature, working with thermal images is a challenge [1].

Hence, to model scenes with thermal data, early studies predominantly relied on range measurements—e.g. from LiDAR [31], depth cameras [53, 48] or even a combination of both sensors [8]—to construct 3D models, onto which thermal information was subsequently projected. However, those approaches require a time-consuming and error-prone manual calibration of sensor transformations,

their precision depends on the accuracy of mapping algorithms, and in the case of depth cameras, are limited by their range. To remove the dependence on range measurements, Maset et al. [39] and De Luis-Ruiz et al. [15] use photogrammetry to construct 3D models from RGB images. While these methods achieve high model accuracy, they depend on a dense set of RGB and thermal images.

While previous works presented in this section rely on range or RGB measurements to build the 3D geometry of a scene, Chen et al. [11] and Sentenac et al. [49] used thermal images for 3D reconstruction and temperature estimation. However, their results are limited to thermal images with high contrast and do not generalize to large structures.

2.2 NeRF and Multimodality

Traditional methods in 3D reconstruction, such as Structure from Motion [46] or Multi-View Stereo [47], depend on dense input data and scenes rich in geometric features. The seminal work by Mildenhall et al. [40] introduced NeRF, enabling the learning of implicit representations of 3D scenes from sparse sets of RGB images for novel view synthesis. Subsequent research efforts have extended and refined the NeRF framework, addressing challenges related to scalability [38], level of detail [2, 4] and efficiency [58].

To enhance scene reconstruction, the first multimodal approach incorporated depth data to guide the learning process [16]. However, recent studies have demonstrated that integrating other modalities—e.g. RGB 2D images and LiDAR 3D point clouds [63] or spectral information from filtered RGB inputs [33]—into NeRF can also yield improved scene representations.

Closely related to our work on thermal imaging, Poggi et al. [44] integrates near-infrared and RGB images to create a composite NIR-RGB 3D scene. However, NIR images share similar features with RGB images, as they are closer to the visible spectrum compared to thermal images.

To the best of our knowledge, ThermoNeRF is the first approach to leverage a NeRF framework for thermal scene representation and novel view synthesis from a sparse set of images. Unlike existing methods that rely on multimodal data with salient visual features, ThermoNeRF combines RGB and thermal features to learn consistent scene geometries across both sensor modalities, while avoiding contamination from each modality in the rendered views.

3 Preliminary

NeRF [40] learns an implicit scene representation as a continuous 5D vector-valued function, mapping a 3D position $\mathbf{x} = (x, y, z)$ and a viewing direction $\mathbf{d} = (\theta, \phi)$ to a color c and a volume density σ . This mapping is applied along rays projected in space from each pixel of an image captured by a camera at pose (\mathbf{x}, \mathbf{d}) . NeRF comprises two Multi-Layer Perceptron (MLP) networks: one predicts the density based solely on the 3D location, and the other predicts color based on the 3D location and the viewing direction, making the color prediction

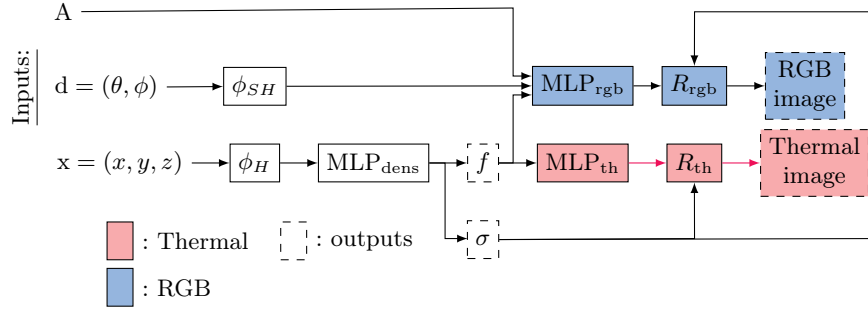


Fig. 2: The proposed ThermoNeRF architecture; in red are the parts of the network related to the generation of thermal images, while blue represents the part related to the generation of RGB images. To ensure that temperature is independent of the viewing direction and appearance, the thermal MLP_{th} takes only the intermediate features f as input.

view-dependent to account for non-Lambertian effects on surfaces. Finally, to reconstruct a view, rays are sampled through the scene, and the color of each ray is rendered using volume rendering techniques.

Nerfacto [50] is a recent extension of NeRF that integrates components from several state-of-the-art models, such as MIP-NeRF [2], MIP-NeRF 360 [3], Instant-NGP [41] and NeRF-W [38], amongst others. The model’s inputs include an additional appearance embedding, which is a per-image embedding that accounts for differences in exposure and lighting conditions across different training views. Furthermore, sinusoidal-based positional encoding is replaced with hash encoding for positions and spherical harmonics for viewing direction. Hence, Nerfacto is defined as follows:

$$\begin{aligned} [\sigma, f] &= \text{MLP}_{\text{dens}}(\phi_H(\mathbf{x})), \\ c &= \text{MLP}_{\text{rgb}}(f, \phi_{SH}(\mathbf{d}), A), \end{aligned} \quad (1)$$

where f are intermediate features, c is colors, $\phi_H(\cdot)$ denotes the hash encoding, $\phi_{SH}(\cdot)$ is the spherical harmonics encoding and A represents the appearance embeddings.

Additionally, Nerfacto uses pose refinement to further optimise the poses predicted for every view. It uses a piecewise sampler to balance sampling through the fine details of the scene and the distant views, and a proposal sampler that emphasizes the density regions of the scene which impact reconstruction quality the most. ThermoNeRF extends Nerfacto to allow reconstruction as well as novel view synthesis of thermal and RGB images.

4 ThermoNeRF

In this section, we present ThermoNeRF, a NeRF model capable of learning an implicit scene representation in both thermal and RGB, from a sparse set



Fig. 3: Illustration of the difference between RGB and thermal images. Non-Lambertian effects—i.e. light reflections—present in the RGB images (left) depend on the angle of view and are not present in thermal images (right). Furthermore, textures and edge features in the thermal images are soft due to the ghosting effect, as opposed to the sharpness of the RGB image and its background.

of RGB and thermal images. To synthesize realistic and accurate RGB and thermal novel views, ThermoNeRF retains geometric features captured by the RGB modality, while ensuring that temperature estimates are independent of scene color variations. Our design choices are guided by two properties of thermal images: 1) Thermal images are inherently *soft and textureless*. 2) Temperatures are *independent of the viewing direction*.

Refer to Fig. 2 for a flowchart of the method; implementation of the model and evaluations can be found online³.

4.1 Thermal Image Rendering

As depicted in Fig. 3, while RGB information can be view-dependent due to non-Lambertian effects, thermal cameras measure thermal radiation and convert it to temperature, which is invariant with respect to the viewing direction. Therefore, ThermoNeRF uses separate MLPs for each modality: MLP_{th} predicts temperatures along each ray, while MLP_{rgb} predicts RGB values. Since temperatures are independent of the viewing direction, MLP_{th} only takes the intermediate features f of MLP_{dens} as input, while MLP_{th} receives f , ϕ_{SH} and A —as presented in Sec. 3.

Furthermore, as seen in the thermal images in Fig. 3, the ghosting effect makes thermal images soft and textureless. Consequently, although textures and sharp geometric features in RGB images allow NeRF models to accurately estimate scene density, NeRF struggles to learn densities solely from thermal images—see Fig. 4b for experimental results of training Nerfacto on thermal images only. Therefore, in ThermoNeRF, a single density MLP_{dens} is shared by the modalities, enabling the network to construct a geometric representation informed by RGB information while ensuring geometric consistency with thermal modality information.

Formally, ThermoNeRF is defined as follows:

³ <https://github.com/SchindlerEPFL/thermo-nerf>

$$\begin{aligned}
[\sigma, f] &= \text{MLP}_{\text{dens}}(\phi_H(\mathbf{x})), \\
c &= \text{MLP}_{\text{rgb}}(f, \phi_{SH}(d), A), \\
t &= \text{MLP}_{\text{th}}(f)
\end{aligned}
\tag{2}$$

where t denotes the predicted temperature values.

4.2 Loss Functions

We use separate reconstruction loss functions for each modality. The final reconstruction loss \mathcal{L} is expressed as the sum of the Mean Square Error (MSE) losses of the RGB and thermal outputs, respectively denoted \mathcal{L}_{rgb} and \mathcal{L}_{th} . Similar to Nerfacto, we add the interlevel and distortion losses, which were initially used in MIP-NeRF 360 [3], to optimize the proposal sampler and to reduce distortions respectively. Therefore, our final loss is defined as follows:

$$\mathcal{L} = \mathcal{L}_{\text{rgb}} + \mathcal{L}_{\text{th}} + \mathcal{L}_{\text{dist}} + \mathcal{L}_{\text{interl.}} \tag{3}$$

5 ThermoScenes Dataset

To evaluate RGB+thermal reconstruction and novel view synthesis methods, we have collected ThermoScenes, a new dataset comprising paired RGB and thermal images for ten scenes (four outdoor and six indoor) with diverse temperature ranges. To collect this dataset, we used a FLIR One Pro LT [21], a dual RGB and thermal camera, mounted on an iPhone, capable of simultaneously capturing aligned pairs of RGB and thermal images. The FLIR One Pro LT thermal camera operates within a range of $-20\text{ }^{\circ}\text{C}$ to $120\text{ }^{\circ}\text{C}$, with a thermal accuracy of $\pm 3\text{ }^{\circ}\text{C}$. In our study, evaluating the quality of 3D thermal reconstruction requires not only understanding the thermal accuracy but also the thermal precision of the camera. We assess the precision to be approximately $\pm 0.14\text{ }^{\circ}\text{C}$. To calculate the precision of our thermal camera, we fix the camera at a position and capture 20 consecutive images of a RaspberryPi connected to power for at least 10 minutes to ensure thermal stability. Our precision is then the average standard deviation of the temperatures of each pixel across the 20 images.

Furthermore, the FLIR software generates thermal images by overlaying thermal information onto RGB features—such as edges—using Multi-Spectral Dynamic Imaging (MSX) [55]. For this dataset, we extract raw thermal data from MSX images using the FLIR Image Extractor library [20], and disregard the MSX-enhanced images.

Tab. 1 provides a summary of the collected ThermoScenes dataset, where each scene is illustrated by two example views in RGB and thermal respectively. The test set for each scene comprises one-eighth of the total number of images, with test views uniformly sampled across the collected camera poses. The minimum and maximum measured temperatures are also reported. More images for all ten scenes, along with a thorough explanation of each scene, are included in

Table 1: Summary of the collected ThermoScenes dataset showing example views with paired RGB and thermal images, the number of train/test views and the temperature range for each scene.

Scene	RGB	Thermal	#views	Temp. range	Scene	RGB	Thermal	#views	Temp. range
Heated Water Cup			95 (train) 13 (test)	23.8°C 68.6°C	Hot Water Kettle			77 (train) 10 (test)	20.0°C 87.3°C
Frozen Ice Cup			133 (train) 19 (test)	-16.2°C 23.1°C	Melting Ice Cup			85 (train) 12 (test)	0.4°C 25.5°C
Building (Spring)			107 (train) 15 (test)	-62.5°C* 19.7°C	Building (Winter)			84 (train) 12 (test)	-15.7°C 15.6°C
Double Robot			83 (train) 11 (test)	21.0°C 29.3°C	Raspberry Pi			111 (train) 15 (test)	22.3°C 41.8°C
Exhibition Building			119 (train) 16 (test)	-11.3°C 14.0°C	Trees			73 (train) 10 (test)	-8.4°C 11.8°C

*In one scene, the sensor outputs values outside of its operating range, which are detected on the clear sky. Due to the variations of atmospheric radiation in the sky, the readings of thermal cameras are subject to systematic inaccuracies [30]. We clip these values to the minimum of the operating range of the camera (-20°C). However, our data can be post-processed for more accurate temperature estimates in the sky [30, 61].

the Dataset Description section of the supplementary material. ThermoScenes is publicly available⁴.

6 Experiments

We conduct a comprehensive evaluation of the quality of rendered novel views using the ThermoScenes dataset introduced in Section 5. This section details the evaluation metrics, compares baselines, and discusses experimental results and ablation studies.

6.1 Evaluation Metrics

Temperature Metrics. We assess the accuracy of the rendered temperatures by computing the Mean Absolute Error (MAE) against the ground-truth thermal view. Given that thermal images often display uniform temperature distributions

⁴ <https://drive.google.com/drive/folders/1Je6pyQUV3keCStn1yLsyyPEd1ccm70B3>

outside the regions of interest, calculating the MAE across the entire image may disproportionately emphasize the ambient background temperature. From an application standpoint, the temperature of the region of interest (ROI) is often crucial for temperature assessment [7]. Therefore, we also report the MAE_{roi} , the MAE computed over the region of interest. We use Otsu’s method [42] to determine the optimal threshold that distinguishes the region-of-interest pixels from the background in thermal images.

Image Quality Metrics. We report the image quality metrics Peak-Signal-to-Noise-Ratio (PSNR) [23] and Structural Similarity Metric (SSIM) [54] for both thermal and RGB modalities. For the RGB views, we include the Learned Perceptual Image Patch Similarity (LPIPS) [60], which is specifically designed to evaluate the human-perceived similarity for RGB images.

6.2 Baselines

We conduct experiments to evaluate the two design choices of our method, i.e. (1) the necessity of multimodality, as thermal images alone cannot accurately estimate the scene density due to lack of texture details, and (2) the decoupling of the RGB and thermal modalities, stemming from the physical independence between temperature and color information. Given that ThermoNeRF is based on Nerfacto, we define two baseline methods derived from Nerfacto: $\text{Nerfacto}_{\text{th}}$ and $\text{Nerfacto}_{\text{rgb+th}}$.

$\text{Nerfacto}_{\text{th}}$ is trained exclusively with thermal inputs (without RGB). It processes thermal images as single-channel grayscale images through Nerfacto’s standard pipeline. This baseline is designed to highlight the importance of incorporating the RGB modality.

$\text{Nerfacto}_{\text{rgb+th}}$ takes both RGB and thermal modalities as inputs by concatenating them into four-channel images and optimizes the concatenated RGB-thermal images without employing separate MLPs for optimizing each modality. This baseline is designed to show the difference between simply concatenating the modalities versus optimizing them separately with a dedicated MLP for each.

6.3 Implementation Details

We train ThermoNeRF as well as our baselines for 30k iterations with 4096 rays per batch. We use a learning rate of 10^{-2} with exponential decay decreasing the learning rate by an order of magnitude to 10^{-3} . The total training time is around 40 minutes using a single T4 GPU.

6.4 Thermal View Synthesis

Tab. 2 provides a comparative analysis of our method’s performance for novel view synthesis in the thermal modality, across the ten scenes of the ThermoScenes dataset.

Temperature Metrics. Tab. 2 reports the average per-pixel MAE_{roi} and MAE of thermal views synthesis on the test set. With an average MAE of 0.66°C ,

Table 2: Quantitative comparison of our method (ThermoNeRF) versus Nerfacto_{th} and Nerfacto_{rgb+th} on thermal novel view synthesis across the ten scenes in ThermoScenes. ThermoNeRF outperforms other methods across all metrics for image quality (PSNR, SSIM) and temperature estimation (MAE_{roi}, MAE).

Metric	Method	Heated		Freezing		Melting		Building		Double Raspberry		Exhibition		Trees	Avg
		Water Cup	Water Kettle	Ice Cup	Ice Cup	(Spring)	(Winter)	Robot	Pi	Building	Building				
PSNR ↑	Nerfacto _{th}	23.68	29.25	23.34	18.50	20.30	22.80	10.49	18.08	23.88	20.91	21.12			
	Nerfacto _{rgb+th}	29.76	31.80	22.9	32.70	20.60	28.47	29.82	24.3	27.74	31.48	27.96			
	ThermoNeRF	32.05	34.04	30.67	32.24	26.63	28.75	30.75	31.80	33.79	31.07	31.18			
SSIM ↑	Nerfacto _{th}	0.71	0.89	0.95	0.93	0.91	0.87	0.45	0.71	0.94	0.92	0.83			
	Nerfacto _{rgb+th}	0.83	0.91	0.96	0.98	0.89	0.89	0.89	0.82	0.95	0.94	0.91			
	ThermoNeRF	0.92	0.94	0.97	0.98	0.92	0.88	0.95	0.96	0.97	0.94	0.94			
MAE _{roi} ↓	Nerfacto _{th}	13.57	5.18	6.75	12.27	6.36	1.80	2.85	4.82	1.29	1.60	5.65			
	Nerfacto _{rgb+th}	5.35	3.25	10.33	1.26	6.54	0.86	1.06	1.62	1.00	0.31	3.16			
	ThermoNeRF	2.10	2.76	3.26	1.57	1.88	0.66	0.91	1.28	0.31	0.25	1.50			
MAE ↓	Nerfacto _{th}	1.82	4.19	1.67	1.97	6.74	1.87	5.33	2.25	1.56	1.49	2.89			
	Nerfacto _{rgb+th}	0.87	1.54	2.01	0.46	6.59	0.89	0.55	1.15	0.97	0.34	1.54			
	ThermoNeRF	0.53	0.71	0.57	0.29	2.40	0.76	0.34	0.27	0.35	0.33	0.66			

ThermoNeRF significantly outperforms Nerfacto_{rgb+th} (1.54°C) and Nerfacto_{th} (2.89°C). When trained on thermal images alone, Nerfacto_{th} fails to learn an accurate representation of the scene (as visible in Fig. 4) and has the lowest image quality and temperature estimation results. On the other hand, thanks to the concatenation of RGB and thermal information, Nerfacto_{rgb+th} obtains better results than Nerfacto_{th}. This is especially visible on the ROI with an average MAE_{roi} of 3.16°C, against 5.65°C for Nerfacto_{th}. However, the estimated temperatures are impacted by the joint optimization of both modalities in the same MLP, as evidenced in Fig. 5 where the error in temperature prediction is high on the region of interest. On the contrary, across the ten scenes, the average MAE_{roi} and MAE for ThermoNeRF are 1.5°C and 0.66°C, respectively, marking a significant improvement over the second-best result of 3.16°C and 1.54°C.

Image Quality Metrics. ThermoNeRF achieves either similar or significantly better results than Nerfacto_{rgb+th} for both the PSNR and SSIM metrics, with a PSNR and SSIM of 31.18 and 0.94, against 27.96 and 0.91 for Nerfacto_{rgb+th}. Using only thermal images results in the lowest PSNR and SSIM (21.12 and 0.83 respectively), highlighting the importance of using both modalities.

In conclusion, the proposed ThermoNeRF architecture brings an improvement of over 50% in temperature estimation, and improved or similar PSNR and SSIM, compared to the second-best model, across various outdoor and indoor scenes.

We visually compare examples of test views rendered by each of the baseline methods as well as by ThermoNeRF (see Fig. 4). We observe noisy renderings with Nerfacto_{th}, while Nerfacto_{rgb+th} generates sensible reconstruction of the geometry—some scenes such as the Double Robot scene being noisier than others. However, temperature predictions are influenced by the RGB modality, leading to biased temperature values and sharper edges compared to the ground truth for the Building (Spring). Moreover, we can see in the rendered thermal images, elements from the RGB view that are invisible in the ground truth thermal

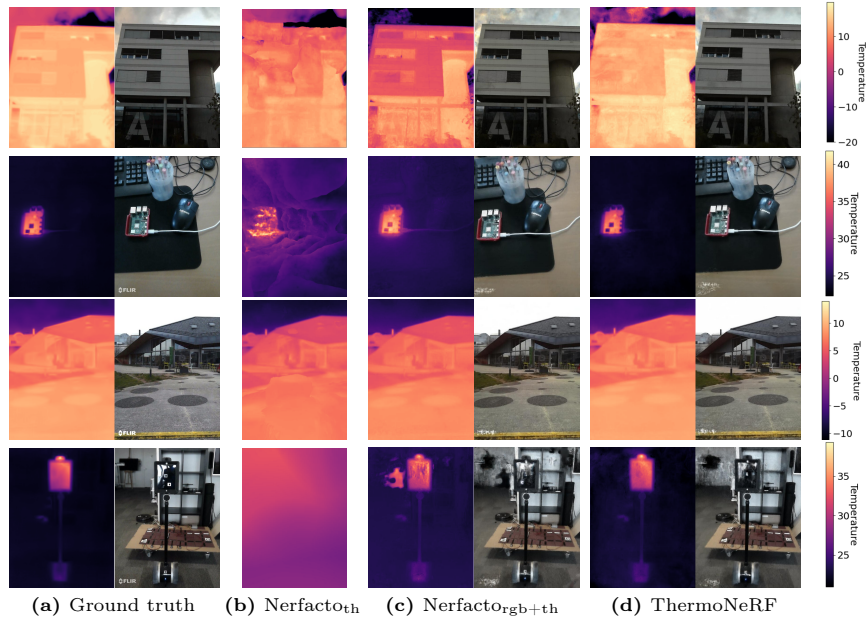


Fig. 4: Comparison of examples of thermal and RGB renderings of unseen poses for the scenes Building (Spring), Raspberry Pi, Exhibition Building and Double Robot. Note that $\text{Nerfacto}_{\text{th}}$ has no RGB output and thus we only show a thermal rendering. ThermoNeRF is closest to the ground-truth thermal image, while preserving RGB quality.

images—this is especially visible in the Raspberry Pi scene with the mouse and keyboard (Fig. 4c). This indicates that the RGB channels have influenced the temperature estimates, as both modalities are optimized within the same MLP. Similar renderings for all ten datasets are shown in the Results section of the supplementary material.

In Fig. 5, where we visualize the per-pixel absolute errors in temperature prediction, we observe highest errors for all models at the edges. This is due to the ghosting effect available in thermal images where the edges are blurry. We also can observe that for Building (Spring) (top-left), the sky has more errors than the Exhibition Building scene (top-right). That is due to having a mix of clear sky and cloudy images on the Building (Spring) scene, as opposed to just a cloudy sky in the Exhibition Building scene. The inconsistencies of thermal radiation measured from the sky leading to less accurate thermal predictions. Overall, ThermoNeRF exhibits the best thermal prediction results while $\text{Nerfacto}_{\text{th}}$ shows the worst thermal predictions as its reconstructions is very distorted. $\text{Nerfacto}_{\text{rgb+th}}$ shows higher errors across the scenes than ThermoNeRF due to the contamination of the thermal information by the RGB as both modalities are optimised in a single MLP.

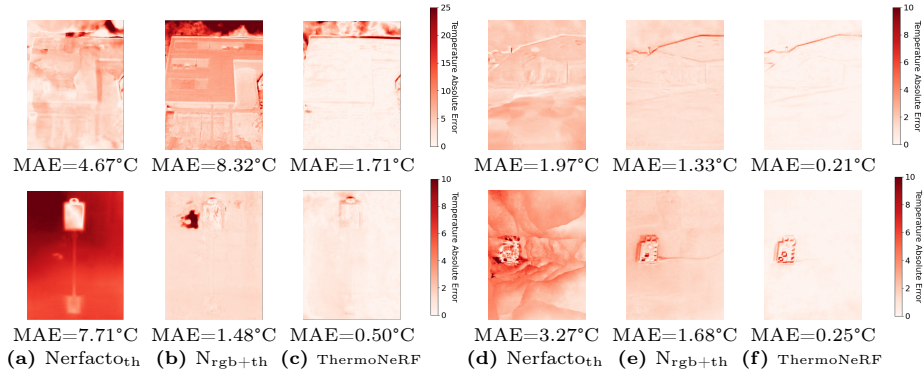


Fig. 5: Comparison of per-pixel absolute errors in temperature estimation for renderings of unseen poses for two outdoor scenes: (top) Building (Spring) and Exhibition Building and two indoor scenes: Double Robot and RaspberryPi (bottom). We observe fewer errors on ThermoNeRF than the baselines. Note that $N_{\text{rgb}+\text{th}}$ stands for $N_{\text{erfacto}_{\text{rgb}+\text{th}}}$.

Table 3: Quantitative comparison of the rendered RGB views between our method (ThermoNeRF) and a Nerfacto trained only with RGB inputs across the ten scenes in ThermoScenes. One can observe that the quality of RGB views obtained with ThermoNeRF is not significantly degraded by the multimodal learning.

Metric	Method	Heated	Heated	Freezing	Melting	Building	Building	Double	Raspberry	Exhibition	Trees	Avg
		Water Cup	Water Kettle	Ice Cup	Ice Cup	(Spring)	(Winter)	Robot	Pi	Building		
PSNR \uparrow	Nerfacto (RGB)	18.11	23.00	24.71	17.97	19.88	20.02	19.05	19.36	22.18	20.37	20.46
	ThermoNeRF	18.16	21.05	25.69	16.20	19.30	19.74	19.02	19.07	22.81	18.67	19.97
	Difference	+0.05	-1.95	+0.98	-1.77	-0.58	-0.28	-0.03	-0.29	+0.83	-1.70	-0.49
SSIM \uparrow	Nerfacto (RGB)	0.53	0.75	0.73	0.52	0.64	0.62	0.65	0.73	0.64	0.67	0.65
	ThermoNeRF	0.56	0.60	0.77	0.43	0.63	0.61	0.65	0.72	0.66	0.59	0.62
	Difference	+0.03	-0.15	+0.04	-0.09	-0.02	-0.01	0.00	-0.01	+0.02	-0.08	-0.03
LPIPS \downarrow	Nerfacto (RGB)	0.25	0.23	0.42	0.17	0.24	0.34	0.28	0.18	0.24	0.32	0.27
	ThermoNeRF	0.25	0.24	0.37	0.18	0.27	0.34	0.30	0.19	0.24	0.35	0.27
	Difference	0.00	+0.01	-0.08	+0.01	+0.03	0.00	+0.02	+0.01	0.00	+0.03	0.00

6.5 RGB View Synthesis

To assess novel view synthesis with ThermoNeRF in the RGB modality, we investigate whether there is a significant degradation in the quality of RGB views compared with the standard Nerfacto trained only on the RGB inputs. Tab. 2 summarises the results, showing little to no degradation in the quality of the RGB views. Indeed, the differences between the PSNR, SSIM and LPIPS of Nerfacto and ThermoNeRF in RGB are -0.49 , -0.03 and 0.00 , respectively.

6.6 Ablation Study

In this section, we conduct an ablation study to evaluate the training strategy of our proposed method. Since ThermoNeRF decouples the MLPs for RGB and thermal modalities, the ablation experiments are designed to assess our fully

joint training strategy—especially, as opposed to sequential training strategies in which the model is first trained on RGB data and then fine-tuned using thermal data. We compare three different strategies, trained over ThermoScenes:

Strategy A initially trains the model using RGB data for 30k iterations, and then fine-tunes the model using thermal data for 30k more iterations. Hence, MLP_{th} is frozen for the first half of the training period, directing the density optimisation to rely entirely on the RGB modality. In the second half of the training, MLP_{rgb} is frozen, and the remaining MLPs are trained for 30k iterations.

Strategy B never uses thermal information to train MLP_{dens} , which relies solely on RGB data. Similar to the structure of strategy A, strategy B involves freezing MLP_{th} throughout the first half of the training period. However, in the second half, both MLP_{dens} and MLP_{rgb} are frozen.

Strategy C initially trains using only RGB data, before training RGB and thermal modalities together. For strategy C, MLP_{th} remains frozen during the first half of the training, similar to the previous cases. However, unlike the earlier strategies, this case involves joint fine-tuning of all modalities during the latter 30k iterations.

We compare the three training strategies with our proposed ThermoNeRF strategy, which jointly trains all modalities for 30k iterations.

Tab. 4 summarises the strategies explored and presents the results for the thermal and RGB modalities with each training strategy, averaged across the ten scenes of ThermoScenes. We report average PSNR, SSIM, MAE_{roi} and MAE for thermal views on the test sets, as well as PSNR, SSIM, and LPIPS for RGB views using the same test poses. Refer to Ablations section of the appendix for per-scene results. The results demonstrate that ThermoNeRF is the most effective training strategy. Additionally, the findings indicate that density cannot be effectively learned on one modality and then transferred to another without additional joint fine-tuning. More specifically, strategy A has an MAE_{roi} of 7.38°C , 6.11°C more than ThermoNeRF. This highlights that relying solely on thermal images is insufficient, even if the density has already been optimised with the RGB modality. Optimising thermal information alone without re-optimising the density, as done in strategy B, leads to increasing the thermal prediction error in the ROI by 7.03°C compared to ThermoNeRF, on average. On the other hand, strategy’s MAE_{roi} is 2.02°C , an increase in error of 0.75°C compared to ThermoNeRF. While strategy C demonstrates that joint training outperforms other disjoint training strategies, it does not validate the effectiveness of first training using the RGB data followed by multimodal fine-tuning.

7 Conclusion

In this work, we propose ThermoNeRF, a novel multimodal approach leveraging Neural Radiance Fields (NeRF) for rendering novel RGB and thermal views of a scene. Additionally, we have curated a new dataset specifically designed for RGB+thermal scene reconstruction.

Table 4: Average metrics results for different training and freezing strategies for each MLP. Strategies A, B and C are ablations of our proposed ThermoNeRF with fully-joint multimodal RGB and thermal training. We have two phases of training—each lasting 30k iterations—and indicate which MLPs are trained ✓ or frozen ✱ in each phase.

Strategy	0 → 30k iterations			30k → 60k iterations			Thermal				RGB		
	MLP _{dens}	MLP _{rgb}	MLP _{th}	MLP _{dens}	MLP _{rgb}	MLP _{th}	PSNR ↑	SSIM ↑	MAE _{roi} ↓	MAE ↓	PSNR ↑	SSIM ↑	LPIPS ↓
A	✓	✓	✱	✓	✱	✓	22.26	0.79	7.38	1.45	12.44	0.35	0.74
B	✓	✓	✱	✱	✱	✓	21.61	0.85	8.30	2.13	11.19	0.39	0.80
C	✓	✓	✱	✓	✱	✓	29.52	0.90	2.02	0.87	19.78	0.61	0.31
ThermoNeRF	✓	✓	✓	-	-	-	31.18	0.94	1.27	0.66	19.97	0.62	0.27

To compensate for the absence of texture in thermal images, our approach leverages paired RGB and thermal data throughout the training process. While the scene density is effectively learned from RGB and thermal inputs by a shared MLP, distinct networks are applied to estimate color and temperature information. Our experimental findings reveal that ThermoNeRF excels in synthesizing thermal images, achieving an average mean absolute error of just 1.5°C, representing more than 50% improvement over a baseline concatenating the RGB and thermal modalities. Moreover, we show our multimodal approach is not detrimental to the quality of the resulting RGB views. Finally, an ablation study demonstrates that ThermoNeRF’s fully-joint multimodal training is more effective than several alternative disjoint training strategies.

An compelling avenue for future research is exploring the adaptability of ThermoNeRF across different frameworks. Although our present work builds upon Nerfacto, investigating ThermoNeRF’s compatibility with recent anti-aliasing NeRF variants, such as ZIP-NeRF [4], presents an interesting opportunity to assess its flexibility and potential for broader application.

Furthermore, a potential limitation of our method is its dependence on paired RGB and thermal images. Collecting such paired RGB-thermal images can pose practical challenges, especially depending on the available hardware. While RGB+thermal cameras—similar to the one used in our experiments—are accessible and cost-effective, using separate RGB and thermal cameras requires careful calibration to align these modalities accurately. Future work will focus on developing a method that allows to train ThermoNeRF using unpaired RGB and thermal image data.

References

1. Bao, F., Jape, S., Schramka, A., Wang, J., McGraw, T.E., Jacob, Z.: Why are thermal images blurry, (2023). eprint: 2307.15800 (physics.optics) (cit. on pp. 2, 3).
2. Barron, J.T., Mildenhall, B., Tancik, M., Hedman, P., Martin-Brualla, R., Srinivasan, P.P.: Mip-NeRF: A Multiscale Representation for Anti-Aliasing Neural Radiance Fields. ICCV (2021) (cit. on pp. 4, 5)

3. Barron, J.T., Mildenhall, B., Verbin, D., Srinivasan, P.P., Hedman, P.: Mip-NeRF 360: Unbounded Anti-Aliased Neural Radiance Fields. *CVPR* (2022) (cit. on pp. 5, 7)
4. Barron, J.T., Mildenhall, B., Verbin, D., Srinivasan, P.P., Hedman, P.: Zip-NeRF: Anti-Aliased Grid-Based Neural Radiance Fields. *ICCV* (2023) (cit. on pp. 4, 14)
5. Berg, A., Ahlberg, J., Felsberg, M.: A thermal infrared dataset for evaluation of short-term tracking methods. In: *Swedish Symposium on image analysis* (2015) (cit. on p. 2)
6. Berg, A., Ahlberg, J., Felsberg, M.: A thermal object tracking benchmark. In: *2015 12th IEEE International Conference on Advanced Video and Signal Based Surveillance (AVSS)*, pp. 1–6 (2015) (cit. on p. 3)
7. Brooke, C.: Thermal Imaging for the Archaeological Investigation of Historic Buildings. *Remote Sensing* **10**(9) (2018) (cit. on p. 9). <https://doi.org/10.3390/rs10091401>. <https://www.mdpi.com/2072-4292/10/9/1401>
8. Campione, I., Lucchi, F., Santopoli, N., Seccia, L.: 3D Thermal Imaging System with Decoupled Acquisition for Industrial and Cultural Heritage Applications. *Applied Sciences* **10**(3), 828 (2020) (cit. on p. 3). <https://doi.org/10.3390/app10030828>. <https://www.mdpi.com/2076-3417/10/3/828> (visited on 02/26/2024)
9. Chang, W., Zhang, Y., Xiong, Z.: Depth Estimation From Indoor Panoramas With Neural Scene Representation. In: *Proceedings of the IEEE/CVF Conference on Computer Vision and Pattern Recognition (CVPR)*, pp. 899–908 (2023) (cit. on p. 1)
10. Chen, C., Richard, A., Shapovalov, R., Ithapu, V.K., Neverova, N., Grauman, K., Vedaldi, A.: Novel-view acoustic synthesis. In: *Proceedings of the IEEE/CVF Conference on Computer Vision and Pattern Recognition*, pp. 6409–6419 (2023) (cit. on p. 1)
11. Chen, C.-Y., Yeh, C.-H., Chang, B.R., Pan, J.-M.: 3D Reconstruction from IR Thermal Images and Reprojective Evaluations. *Mathematical Problems in Engineering* **2015**, e520534 (2015) (cit. on p. 4). <https://doi.org/10.1155/2015/520534>. <https://www.hindawi.com/journals/mpe/2015/520534/> (visited on 02/14/2024)
12. Cho, Y., Bianchi-Berthouze, N., Marquardt, N., Julier, S.J.: Deep Thermal Imaging: Proximate Material Type Recognition in the Wild through Deep Learning of Spatial Surface Temperature Patterns. In: *Proceedings of the 2018 CHI Conference on Human Factors in Computing Systems. CHI '18. ACM* (2018) (cit. on p. 2). <https://doi.org/10.1145/3173574.3173576>
13. Choi, Y., Kim, N., Hwang, S., Park, K., Yoon, J.S., An, K., Kweon, I.S.: KAIST Multi-Spectral Day/Night Data Set for Autonomous and Assisted Driving. *IEEE Transactions on Intelligent Transportation Systems* **19**(3), 934–948 (2018) (cit. on p. 2). <https://doi.org/10.1109/TITS.2018.2791533>
14. Dai, W., Zhang, Y., Chen, S., Sun, D., Kong, D.: A Multi-spectral Dataset for Evaluating Motion Estimation Systems, (2021). arXiv: 2007.00622 [cs.CV] (cit. on p. 2).
15. De Luis-Ruiz, J.M., Sedano-Cibrián, J., Pérez-Álvarez, R., Pereda-García, R., Salas-Menocal, R.B.: Generation of 3D Thermal Models for the Analysis of Energy Efficiency in Buildings. In: *Cavas-Martínez, F., Marín Granados, M.D., Mirálbes Buil, R., de-Cózar-Macías, O.D. (eds.) Advances in Design Engineering III*, pp. 741–754. Springer International Publishing, Cham (2023) (cit. on pp. 2, 4)
16. Deng, K., Liu, A., Zhu, J.-Y., Ramanan, D.: Depth-supervised NeRF: Fewer Views and Faster Training for Free. *2022 IEEE/CVF Conference on Computer Vision and*

- Pattern Recognition (CVPR) (2021) (cit. on p. 4). <https://api.semanticscholar.org/CorpusID:235743051>
17. Devaguptapu, C., Akolekar, N., M Sharma, M., N Balasubramanian, V.: Borrow from anywhere: Pseudo multi-modal object detection in thermal imagery. In: Proceedings of the IEEE/CVF Conference on Computer Vision and Pattern Recognition Workshops, pp. 0–0 (2019) (cit. on p. 3)
 18. Farooq, M.A., Shariff, W., Khan, F., Corcoran, P., Rotariu, C.: *C3I Thermal Automotive Dataset*, (2022). <https://doi.org/10.21227/jf21-rt22> (cit. on p. 2).
 19. FLIR, T.: FLIR Thermal Dataset for Algorithm Training, <https://www.flir.com/oem/adas/adas-dataset-form/> (cit. on p. 2).
 20. Flir Image Extractor CLI, <https://pypi.org/project/flirimageextractor/> (cit. on p. 7).
 21. FLIR ONE Pro Thermal Imaging Camera for Smartphones | Teledyne FLIR, <https://www.flir.com/products/flir-one-pro/> (cit. on p. 7).
 22. Gade, R., Moeslund, T.: Thermal cameras and applications: A survey. *Machine Vision and Applications* **25**, 245–262 (2014) (cit. on p. 2). <https://doi.org/10.1007/s00138-013-0570-5>
 23. Horé, A., Ziou, D.: Image Quality Metrics: PSNR vs. SSIM. In: 2010 20th International Conference on Pattern Recognition, pp. 2366–2369 (2010) (cit. on p. 9). <https://doi.org/10.1109/ICPR.2010.579>
 24. Hu, B., Huang, J., Liu, Y., Tai, Y.-W., Tang, C.-K.: NeRF-RPN: A general framework for object detection in NeRFs. In: Proceedings of the IEEE/CVF Conference on Computer Vision and Pattern Recognition, pp. 23528–23538 (2023) (cit. on p. 1)
 25. Hu, L., Delichatsios, M.: “Thermal Radiation”. In: *Encyclopedia of Wildfires and Wildland-Urban Interface (WUI) Fires*. Ed. by S.L. Manzello. Cham: Springer International Publishing, 2019, pp. 1–8. ISBN: 978-3-319-51727-8. https://doi.org/10.1007/978-3-319-51727-8_78-1 (cit. on p. 3).
 26. Hwang, S., Park, J., Kim, N., Choi, Y., Kweon, I.: Multispectral Pedestrian Detection: Benchmark Dataset and Baseline. In: (2015) (cit. on p. 2). <https://doi.org/10.1109/CVPR.2015.7298706>
 27. Janssens, O., Van de Walle, R., Loccufer, M., Van Hoecke, S.: Deep learning for infrared thermal image based machine health monitoring. *IEEE/ASME Transactions on Mechatronics* **23**(1), 151–159 (2017) (cit. on p. 3)
 28. Kim, H., Lamichhane, N., Kim, C., Shrestha, R.: Innovations in Building Diagnostics and Condition Monitoring: A Comprehensive Review of Infrared Thermography Applications. *Buildings* **13**(11) (2023) (cit. on p. 2). <https://doi.org/10.3390/buildings13112829>
 29. Kopaczka, M., Kolk, R., Merhof, D.: A fully annotated thermal face database and its application for thermal facial expression recognition. In: 2018 IEEE International Instrumentation and Measurement Technology Conference (I2MTC), pp. 1–6 (2018) (cit. on p. 2). <https://doi.org/10.1109/I2MTC.2018.8409768>
 30. Kruczek, T.: Conditions for use of long-wave infrared camera to measure the temperature of the sky. *Energy* **283**, 128466 (2023) (cit. on p. 8). <https://doi.org/10.1016/j.energy.2023.128466>. <https://www.sciencedirect.com/science/article/pii/S0360544223018601>
 31. Lagüela, S., Martínez, J., Armesto, J., Arias, P.: Energy efficiency studies through 3D laser scanning and thermographic technologies. *Energy and Buildings* **43**(6), 1216–1221 (2011) (cit. on p. 3). <https://doi.org/10.1016/j.enbuild.2010.12.031>. <https://www.sciencedirect.com/science/article/pii/S0378778811000041> (visited on 02/26/2024)

32. Lee, A.J., Cho, Y., Shin, Y.-s., Kim, A., Myung, H.: ViViD++: Vision for visibility dataset. *IEEE Robotics and Automation Letters* **7**(3), 6282–6289 (2022) (cit. on p. 2)
33. Li, J., Li, Y., Sun, C., Wang, C., Xiang, J.: Spec-NeRF: Multi-spectral Neural Radiance Fields, (2023). <https://doi.org/10.48550/arXiv.2310.12987>. <http://arxiv.org/abs/2310.12987> (visited on 02/26/2024). arXiv:2310.12987 [cs, eess] (cit. on p. 4).
34. Liu, F., Zhang, C., Zheng, Y., Duan, Y.: Semantic Ray: Learning a Generalizable Semantic Field with Cross-Reprojection Attention. In: *Proceedings of the IEEE/CVF Conference on Computer Vision and Pattern Recognition*, pp. 17386–17396 (2023) (cit. on p. 1)
35. Liu, S., Gao, M., John, V., Liu, Z., Blasch, E.: Deep learning thermal image translation for night vision perception. *ACM Transactions on Intelligent Systems and Technology (TIST)* **12**(1), 1–18 (2020) (cit. on p. 3)
36. Luo, Q., Gao, B., Woo, W.L., Yang, Y.: Temporal and spatial deep learning network for infrared thermal defect detection. *Ndt & E International* **108**, 102164 (2019) (cit. on p. 3)
37. Martin, M., Chong, A., Biljecki, F., Miller, C.: Infrared thermography in the built environment: A multi-scale review. *Renewable and Sustainable Energy Reviews* **165**, 112540 (2022) (cit. on p. 2). <https://doi.org/10.1016/j.rser.2022.112540>
38. Martin-Brualla, R., Radwan, N., Sajjadi, M.S., Barron, J.T., Dosovitskiy, A., Duckworth, D.: Nerf in the wild: Neural radiance fields for unconstrained photo collections. In: *Proceedings of the IEEE/CVF Conference on Computer Vision and Pattern Recognition*, pp. 7210–7219 (2021) (cit. on pp. 4, 5)
39. Maset, E., Fusiello, A., Crosilla, F., Toldo, R., Zorzetto, D.: PHOTOGRAMMETRIC 3D BUILDING RECONSTRUCTION FROM THERMAL IMAGES. *ISPRS Annals of the Photogrammetry, Remote Sensing and Spatial Information Sciences* **IV-2-W3**, 25–32 (2017) (cit. on pp. 2, 4). <https://doi.org/10.5194/isprs-annals-IV-2-W3-25-2017>. <https://isprs-annals.copernicus.org/articles/IV-2-W3/25/2017/> (visited on 02/26/2024)
40. Mildenhall, B., Srinivasan, P.P., Tancik, M., Barron, J.T., Ramamoorthi, R., Ng, R.: NeRF: Representing Scenes as Neural Radiance Fields for View Synthesis. In: *ECCV* (2020) (cit. on pp. 1, 4)
41. Müller, T., Evans, A., Schied, C., Keller, A.: Instant Neural Graphics Primitives with a Multiresolution Hash Encoding. *ACM Trans. Graph.* **41**(4), 102:1–102:15 (2022) (cit. on p. 5). <https://doi.org/10.1145/3528223.3530127>
42. Otsu, N.: A Threshold Selection Method from Gray-Level Histograms. *IEEE Transactions on Systems, Man, and Cybernetics* **9**(1), 62–66 (1979) (cit. on p. 9). <https://doi.org/10.1109/TSMC.1979.4310076>
43. Parihar, G., Saha, S., Giri, L.I.: Application of infrared thermography for irrigation scheduling of horticulture plants. *Smart Agricultural Technology* **1**, 100021 (2021) (cit. on p. 2). <https://doi.org/10.1016/j.atech.2021.100021>. <https://www.sciencedirect.com/science/article/pii/S2772375521000216>
44. Poggi, M., Ramirez, P.Z., Tosi, F., Salti, S., Mattoccia, S., Stefano, L.D.: Cross-Spectral Neural Radiance Fields. In: *2022 International Conference on 3D Vision (3DV)*, pp. 606–616 (2022) (cit. on pp. 1, 2, 4). <https://doi.org/10.1109/3DV57658.2022.00071>. <https://ieeexplore.ieee.org/abstract/document/10044414> (visited on 02/14/2024)
45. Ramón, A., Adán, A., Javier Castilla, F.: Thermal point clouds of buildings: A review. *Energy and Buildings* **274**, 112425 (2022) (cit. on p. 2). <https://doi.org/>

- 10.1016/j.enbuild.2022.112425. <https://www.sciencedirect.com/science/article/pii/S0378778822005965>
46. Schonberger, J.L., Frahm, J.-M.: Structure-From-Motion Revisited. In: Proceedings of the IEEE Conference on Computer Vision and Pattern Recognition (CVPR) (2016) (cit. on p. 4)
 47. Schönberger, J.L., Zheng, E., Frahm, J.-M., Pollefeys, M.: Pixelwise view selection for unstructured multi-view stereo. In: Computer Vision–ECCV 2016: 14th European Conference, Amsterdam, The Netherlands, October 11–14, 2016, Proceedings, Part III 14, pp. 501–518 (2016) (cit. on p. 4)
 48. Schramm, S., Osterhold, P., Schmoll, R., Kroll, A.: Combining modern 3D reconstruction and thermal imaging: generation of large-scale 3D thermograms in real-time. *Quantitative InfraRed Thermography Journal* **19**(5), 295–311 (2022) (cit. on p. 3). <https://doi.org/10.1080/17686733.2021.1991746>
 49. Sentenac, T., Bugarin, F., Ducarouge, B., Devy, M.: Automated thermal 3D reconstruction based on a robot equipped with uncalibrated infrared stereovision cameras. *Advanced Engineering Informatics* **38**, 203–215 (2018) (cit. on p. 4). <https://doi.org/10.1016/j.aei.2018.06.008>. <https://www.sciencedirect.com/science/article/pii/S1474034617305724> (visited on 02/14/2024)
 50. Tancik, M., Weber, E., Ng, E., Li, R., Yi, B., Wang, T., Kristoffersen, A., Austin, J., Salahi, K., Ahuja, A., McAllister, D., Kerr, J., Kanazawa, A.: Nerfstudio: A Modular Framework for Neural Radiance Field Development. In: Special Interest Group on Computer Graphics and Interactive Techniques Conference Proceedings. SIGGRAPH '23. ACM (2023) (cit. on p. 5). <https://doi.org/10.1145/3588432.3591516>
 51. Tosi, F., Tonioni, A., De Gregorio, D., Poggi, M.: NeRF-Supervised Deep Stereo. In: Proceedings of the IEEE/CVF Conference on Computer Vision and Pattern Recognition, pp. 855–866 (2023) (cit. on p. 1)
 52. Vertens, J., Zürn, J., Burgard, W.: HeatNet: Bridging the Day-Night Domain Gap in Semantic Segmentation with Thermal Images. arXiv preprint arXiv:2003.04645 (2020) (cit. on p. 2)
 53. Vidas, S., Moghadam, P.: HeatWave: A handheld 3D thermography system for energy auditing. *Energy and Buildings* **66**, 445–460 (2013) (cit. on p. 3). <https://doi.org/10.1016/j.enbuild.2013.07.030>. <https://www.sciencedirect.com/science/article/pii/S0378778813004180>
 54. Wang, Z., Bovik, A., Sheikh, H., Simoncelli, E.: Image Quality Assessment: From Error Visibility to Structural Similarity. *Image Processing, IEEE Transactions on* **13**, 600–612 (2004) (cit. on p. 9). <https://doi.org/10.1109/TIP.2003.819861>
 55. What is MSX?, <https://www.flir.com/discover/professional-tools/what-is-msx/> (cit. on p. 7).
 56. Xu, C., Wu, B., Hou, J., Tsai, S., Li, R., Wang, J., Zhan, W., He, Z., Vajda, P., Keutzer, K., Tomizuka, M.: NeRF-Det: Learning Geometry-Aware Volumetric Representation for Multi-View 3D Object Detection. In: Proceedings of the IEEE/CVF International Conference on Computer Vision (ICCV), pp. 23320–23330 (2023) (cit. on p. 1)
 57. Yin, J., Li, A., Li, T., Yu, W., Zou, D.: M2DGR: A Multi-sensor and Multi-scenario SLAM Dataset for Ground Robots. *IEEE Robotics and Automation Letters* (2021) (cit. on p. 2). <https://doi.org/10.1109/LRA.2021.3138527>
 58. Yu, A., Li, R., Tancik, M., Li, H., Ng, R., Kanazawa, A.: Plenotrees for real-time rendering of neural radiance fields. In: Proceedings of the IEEE/CVF International Conference on Computer Vision, pp. 5752–5761 (2021) (cit. on p. 4)

59. Zhang, J., Zhang, F., Kuang, S., Zhang, L.: NeRF-LiDAR: Generating Realistic LiDAR Point Clouds with Neural Radiance Fields. In: AAAI Conference on Artificial Intelligence (AAAI) (2024) (cit. on p. 1)
60. Zhang, R., Isola, P., Efros, A.A., Shechtman, E., Wang, O.: The unreasonable effectiveness of deep features as a perceptual metric. In: Proceedings of the IEEE conference on computer vision and pattern recognition, pp. 586–595 (2018) (cit. on p. 9)
61. Zhao, C., Zhang, L., Zhang, Y.: All-sky longwave radiation modelling based on infrared images and machine learning. *Building and Environment* **238**, 110369 (2023) (cit. on p. 8). <https://doi.org/10.1016/j.buildenv.2023.110369>
62. Zhi, S., Laidlow, T., Leutenegger, S., Davison, A.J.: In-Place Scene Labelling and Understanding with Implicit Scene Representation. In: ICCV (2021) (cit. on p. 1)
63. Zhu, H., Sun, Y., Liu, C., Xia, L., Luo, J., Qiao, N., Nevatia, R., Kuo, C.-H.: Multimodal Neural Radiance Field. In: 2023 IEEE International Conference on Robotics and Automation (ICRA), pp. 9393–9399 (2023) (cit. on pp. 1, 4). <https://doi.org/10.1109/ICRA48891.2023.10160388>